ASSESSMENT OF PIV LOAD-ESTIMATION TECHNIQUES FOR 2D AND 3D BLUFF BODIES

Sajad Maleki Dastjerdi[1,*], Wouter Terra[1], Andrea Sciacchitano[1]

1:Delft University of Technology, Delft, the Netherlands
*Corresponding author: s.malekidastjerdi@tudelft.nl

Keywords: 2D PIV, 3D LPT, load measurements, sensitivity analysis, bluff body.

ABSTRACT

In this study, the accuracy and practical limitations of three PIV-based load-estimation methods are assessed for 2D and 3D bluff-bodies using two-dimensional PIV and three-dimensional Lagrangian particle tracking (LPT) data. The investigated methods are the control-volume (CV) approach, the wake-rake approach, and the total pressure coefficient (CPT) approach. The CV method computes the aerodynamic load by integrating the momentum, Reynolds stress, and pressure contributions over a control surface enclosing the object, whereas the wake-rake and CPT methods estimate drag from downstream wake-plane measurements using the freestream pressure and velocity. Static pressure fields required by the formulations are reconstructed from the measured velocity fields through the pressure Poisson equation. The methods are evaluated using two experimental datasets: planar PIV measurements around a circular cylinder with zig-zag trips at a freestream velocity of 15 m/s, and 3D LPT measurements around a small-scaled time-trial cyclist model. In both cases, the drag coefficients obtained from the methods are compared against reference load balance measurements. The influence of the downstream boundary location is also investigated. For the cylinder case, the CV method shows the highest accuracy, with the drag-coefficient error decreasing below 1% when the downstream boundary is placed sufficiently far from the cylinder. In contrast, the wake-rake and CPT methods exhibit larger errors and tend to underestimate the drag within the available downstream domain. Their accuracy is also strongly affected by the prescribed freestream quantities, particularly U_∞, for which even small bias errors can significantly alter the computed drag. The 3D LPT results around the cyclist model show a similar trend: the CV method stabilizes faster and fluctuates around zero error, whereas the wake-rake and CPT methods continue to decrease toward zero without reaching a fully converged value within the measurement domain. These findings demonstrate that, although the wake-rake and CPT methods require fewer measurement surfaces, they demand accurate freestream conditions and larger downstream measurement regions. Overall, the CV method provides the most reliable load estimation among the methods for bluff bodies when a control volume enclosing the object can be measured.

Nomenclature

Symbols			Greek symbols		
C_D	Drag coefficient	–	μ	Dynamic viscosity	N.s/m^2
C_P	Static pressure coefficient	–	ρ	Fluid density	kg/m^3
C_{PT}	Total pressure coefficient	–	$\nabla^2 P$	Laplacian pressure	Pa/m^2
D	Cylinder diameter	m			
F_i	Time-averaged force component in the i-direction	N	**Subscripts and superscripts**		
L	Bicycle length	m	∞	Freestream quantity	
$n_{i,j}$	Components of the outward unit normal vector to the control surface	–	i, j	Tensor/component indices	
P	Static pressure	Pa	wake	Wake-plane quantity	
P_∞	Freestream pressure	Pa	$\overline{(-)}$	Time-averaged quantity	
P_{total}	Total pressure	Pa	$(-)'$	Fluctuating component	
S	Control-volume surface	m^2	RMS	Root mean square value	
S_{wake}	Wake-plane surface	m^2			
$u_{i,j}$	Velocity components in the i- and j-directions	m/s	**Abbreviations**		
$\overline{u}$	Time-averaged velocity	m/s	CPT	Total pressure coefficient method	
u'	Velocity fluctuations	m/s	CV	Control volume	
u_{RMS}	Root mean square of streamwise velocity fluctuations	m/s	HFSB	Helium-filled soap bubbles	
U_∞	Freestream velocity	m/s	LPT	Lagrangian particle tracking	
$x_{i,j}$	Spatial coordinates	m	PIV	Particle image velocimetry	
X/D	Streamwise distance normalized by cylinder diameter	–			
X/L	Streamwise distance normalized by bicycle length	–			

1. Introduction

Force balances can measure loads with very high accuracy, but they offer no information about the flow physics behind those loads. Surface pressure tapping provides spatial pressure distributions, yet suffers from low spatial resolution and requires expensive, time-consuming model preparation. It is also impractical near thin edges, rotating components, or on living models such as birds [1]. Wake rake measurements using Pitot probes can estimate drag through the momentum deficit, but they are intrusive and limited to one streamwise location. Moreover, they only measure mean dynamic pressure and miss fluctuating components, which can significantly contribute to drag [2].

Particle Image Velocimetry (PIV) has become the chief experimental technique for quantitative flow visualizations in two- or three-dimensional domains. Since the advent of the method, the measured PIV flow fields have been shown to be suitable for evaluating the aerodynamic loads

acting on wind tunnel models via the application of the conservation of momentum in a control volume enclosing the object. The control-volume method, as widely adopted by Van Oudheusden et al. and Limacher et al., is based on integrating the velocity fields surrounding the object to compute the forces, including lift and drag [3], [4], [5]. For computing the forces, the value of the static pressure in the flow is required, which can be computed using the Poisson equation and measured velocity leveraging the Navier-Stokes equations, as discussed in studies such as Gharali and Johnson [6] and Villegas et al. [7] and Fujitawasa et al. [8]. Vorticity-based methods provide an alternative to pressure integration, particularly for cases where near-body velocity data is difficult to capture. Limacher et al. [5] developed the Generalized Added-Mass and Circulatory (GAMC) force formulation, which separates the forces into components related to added-mass and circulatory effects. This method is particularly useful when vorticity fields are available from PIV measurements, offering a robust framework for force computation. Another approach to force estimation from PIV data is the wake rake method, which estimates the aerodynamic forces by measuring the velocity fields downstream of an object. Terra et al. [9] assessed the accuracy of this technique comparing the drag estimated on a full-scale cyclist model to force balance measurements, showing that the PIV wake rake approach has a measurement sensitivity of 30 drag counts. A further advancement of the PIV wake rake approach is the total-pressure method, derived from the former under the assumption that the static pressure in the wake recovers to the freestream value. This method has been shown to offer higher accuracy due to its lower sensitivity to velocity measurement errors [10].

From the reviewed literature, it is evident that, due to the importance of force measurement and the advantages of PIV as a non-intrusive technique, significant efforts have been made to identify the most accurate method for deriving forces from PIV results. However, a key knowledge gap remains, and there is a lack of studies evaluating these methods especially for bluff bodies. Moreover, there is a notable absence of analyses of the sensitivity of these methods, such as the distance between the object and the control volume.

In this study, the accuracy of force measurement approaches from 2D and 3D PIV data around bluff bodies will be evaluated, with a detailed discussion on their reliability and inherent limitations. Moreover, the sensitivity of the methods to variations in the size of the control volume boundary will be assessed comprehensively.

2. Methodology

In this section, the theories and equations used to compute loads from PIV data are first introduced. The experimental setups used to acquire the PIV data are then described in detail.

2.1. PIV load estimation techniques

The time-averaged loads acting on a body immersed in an incompressible fluid can be computed invoking the conservation of momentum in a control volume containing the object. Three different formulations are considered here: the original control volume approach, the wake rake formulation and the total pressure formulation.

Control volume approach (CV): The mean force acting on the object using the control volume approach can be calculated using Eq. (1) [11]:

$$\overline{F}_i = -\rho \iint_S \overline{u}_i \overline{u}_j n_j \, dS - \rho \iint_S \overline{u'_i u'_j} n_j \, dS - \iint_S \overline{p} \, n_i \, dS + \mu \iint_S \left(\frac{\partial \overline{u}_i}{\partial x_j} + \frac{\partial \overline{u}_j}{\partial x_i} \right) n_j \, dS. \tag{1}$$

In this equation, $\overline{F}_i$ is a time-averaged force in direction of i (N) and j is normal direction to the surface S, $\overline{u}$ is the time-averaged velocity (m/s), n is normal vector of the surface, $\overline{p}$ is the time-averaged surface pressure (N/m^2), u' is the velocity fluctuation (m/s), ρ is the fluid density (kg/m^3) and μ is the dynamic viscosity (N.s/m^2). Notice that this approach requires the knowledge of the velocity and of the static pressure all over the surface of the control volume. Also, for high Reynolds number flows and sufficiently large control volumes, the last term of equation (1) is orders of magnitude smaller than the other terms and can be neglected [11].

Wake rake approach: Van Oudheusden et al. [4] showed that the drag force on an object can be determined from the velocity and pressure statistics in the wake of the object if the considered surface in the wake is sufficiently large and the freestream conditions are known. The expression of the time-averaged force reads as [12]:

$$\overline{F}_i = \rho \iint_{S_{wake}} \overline{u} \left(U_\infty - \overline{u} \right) \, dS + \iint_{S_{wake}} \left(p_\infty - \overline{p} \right) \, dS - \rho \iint_{S_{wake}} \overline{u'^2} \, dS. \tag{2}$$

Where U_∞ and P_∞ are the freestream velocity (m/s) and pressure (N/m^2), respectively, and S_{wake} is the surface of the wake plane (m^2). With respect to equation (1), equation (2) relies only on flow measurements in the wake plane, rather than all around the object, provided that the freestream velocity and pressure values are known.

CPT approach: The third method considered here for calculating the aerodynamic force is the total pressure coefficient approach (CPT), described by Eq. (3) [13]. This equation can be derived from the wake rake approach by assuming that the static pressure on the wake surface has recovered to the freestream value.

$$\overline{F}_i = \rho \iint_{S_{wake}} \overline{u} \left(1 - \sqrt{\overline{C_{pt}}} \right) \, dS - \rho \iint_{S_{wake}} \overline{u'^2} \, dS. \tag{3}$$

where C_{pt} is the total pressure coefficient, $C_{pt} = (P_{total} - P_\infty)/(0.5 \rho U_\infty^2)$, with P_{total} the total pressure (N/m^2).

All three approaches contain pressure terms and thus require the evaluation of the static pressure. A common approach for calculating the static pressure from velocity data is through the solution of the Poisson equation for pressure, which for an incompressible, inviscid flow reads as in Eq. (4), imposing appropriate boundary conditions [15].

$$\nabla^2 p = \rho \nabla \cdot (\mathbf{u} \cdot \nabla \mathbf{u}) \,. \tag{4}$$

2.2. Experimental setup and procedures

2D PIV and 3D Lagrangian particle tracking (LPT) experiments were conducted. In both cases, the flow all around the model was measured in order to assess the three load evaluation techniques described in the previous section.

2D-PIV: The experiments were conducted in the M-Tunnel at TU Delft, which is an open-jet open-return wind tunnel. The M-tunnel is capable of generating wind speeds up to 30 m/s, with a test section cross-sectional area of 0.4 m by 0.4 m. Two circular holes in the closed test-section accommodate a fully transparent acrylic cylinder with a diameter of 5 cm and height of 50 cm (Fig. 1), and surface height roughness of about 0.8 μm. As can be seen in Fig. 1(A), the laser is positioned at the exit of the wind tunnel. By employing cylindrical lenses, the laser beam is transformed into a sheet. Fig. 1(A), which is the schematic figure from a 3D view, highlights the placement of critical components within the wind tunnel, including the camera, the load balance, and the smoke generator. Lastly, the actual picture in Fig. 1(B) provides a closer view of the direction of the wind within the test section, along with a detailed depiction of the cylinder. The tests were conducted at a velocity of 15 m/s and zig-zag trips were glued onto the cylinder at an azimuth angle of $\pm 45^{\circ}$, to trigger boundary layer transition prior to the separation [14]. The information about the equipment in the PIV setup is summarized in Table 1. The recorded images were pre-processed by subtracting the sliding minimum intensity over 7 frames to remove the background. Subsequently, a four-pass 2D-PIV cross-correlation algorithm was applied, using interrogation window sizes ranging from 128×128 to 32×32 pixels which is about 27.7×27.7 mm^2 to 7×7 mm^2. Finally, all computed fields were ensemble-averaged through 1000 vector fields, and the RMS components were also evaluated. DaVis 8 was used for the processing raw images.

In addition to the PIV measurements, a 50 N force balance with the accuracy of $\pm 0.1\%$ [16], capable of measuring forces in both X and Y directions, was used to measure the drag force on the cylinder. This provided a benchmark for validating the accuracy of the aerodynamic force evaluated from the PIV results using the mentioned methodologies.

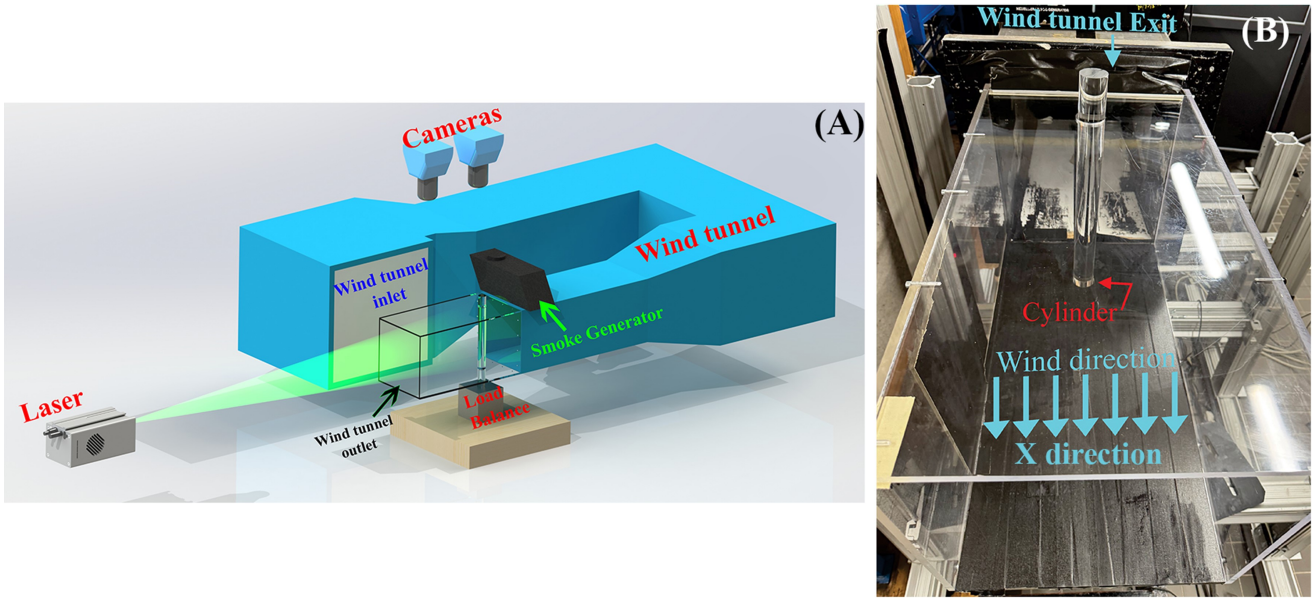


Figure 1. Experimental setup: A) 3D schematic view, B) picture of the test section.

3D-LPT: For the 3D analysis, the flow statistics measured by Hendriksen et al. [17] are used. These experiments were conducted in the open-jet, open-return W-tunnel of the High-Speed Laboratory at the Aerospace Engineering Department of TU Delft. The W-tunnel has a cross-section of 60×60 cm^2 and can reach wind velocities up to 15 m/s. The test object was a small-scale cyclist model, representing an 8-time reduced version of the generic cyclist model in the time-trial position [14], Fig. 2. The model was 3D-printed using black PLA material and was coated with Musou Black, the darkest commercially available paint to minimize reflections during illumination. The object was mounted on a platform with dimensions of 80×80 cm^2, positioned 10 cm above the wind-tunnel exit floor (Fig. 2 to minimize the boundary layers thickness on this false floor. Lagrangian particle tracking was employed, using ten Bobcat cameras, helium-filled soap bubble (HFSB) tracers and four pulsed LEDs. Table 1 summarizes the experiments parameters [17]. Image acquisition and processing was conducted using the LaVision DaVis 10 software. For having a reference for load measured from 3D LPT data, load balance was also connected to the small-scale cyclist from below (similar to the 2D PIV experiment).

The raw images were pre-processed using a time-minimum intensity subtraction, similar to the approach used in 2D-PIV. Particle tracking was then performed using the two-pulse Shake-The-Box algorithm [18]. After obtaining the full set of particle tracks, the data was averaged in cubic bins of 64 voxel size ($14.4 \times 28.1 \times 3.48$ mm^3), using the approach introduced by Aguera et al. (2016).

Table 1. PIV setup information.

		2D PIV	**3D LPT**
Imager	Camera type	1 LaVision sCMOS	2 Antenna with 5 Bobcat cameras
	Resolution	2560×2160 pixels	2 MPx
	Pixel size	6.5 μm	4.4 μm
	Field of view	40×40 cm^2	$42 \times 10 \times 22$ cm^3
	Focal length	35 mm	25 mm
	f#	4	8
	Magnification	0.03	0.02
	Imaging rate	15 Hz, double frame, 500 images per case	8 Hz, double frame
Illumination	Name	Evergreen Nd-YAG laser	LaVision air-cooled LED flashlight 300
	Energy per pulse or Power	200 mJ	300 W
Seeding particles	Name	Ethylene glycol based smoke	Helium-filled soap bubble (HFSB)
	Diameter	1 μm	400 μm
	Supplier	SAFEX seeding generator	TU Delft HFSB rake
Software	Name	DaVis 8	DaVis 10

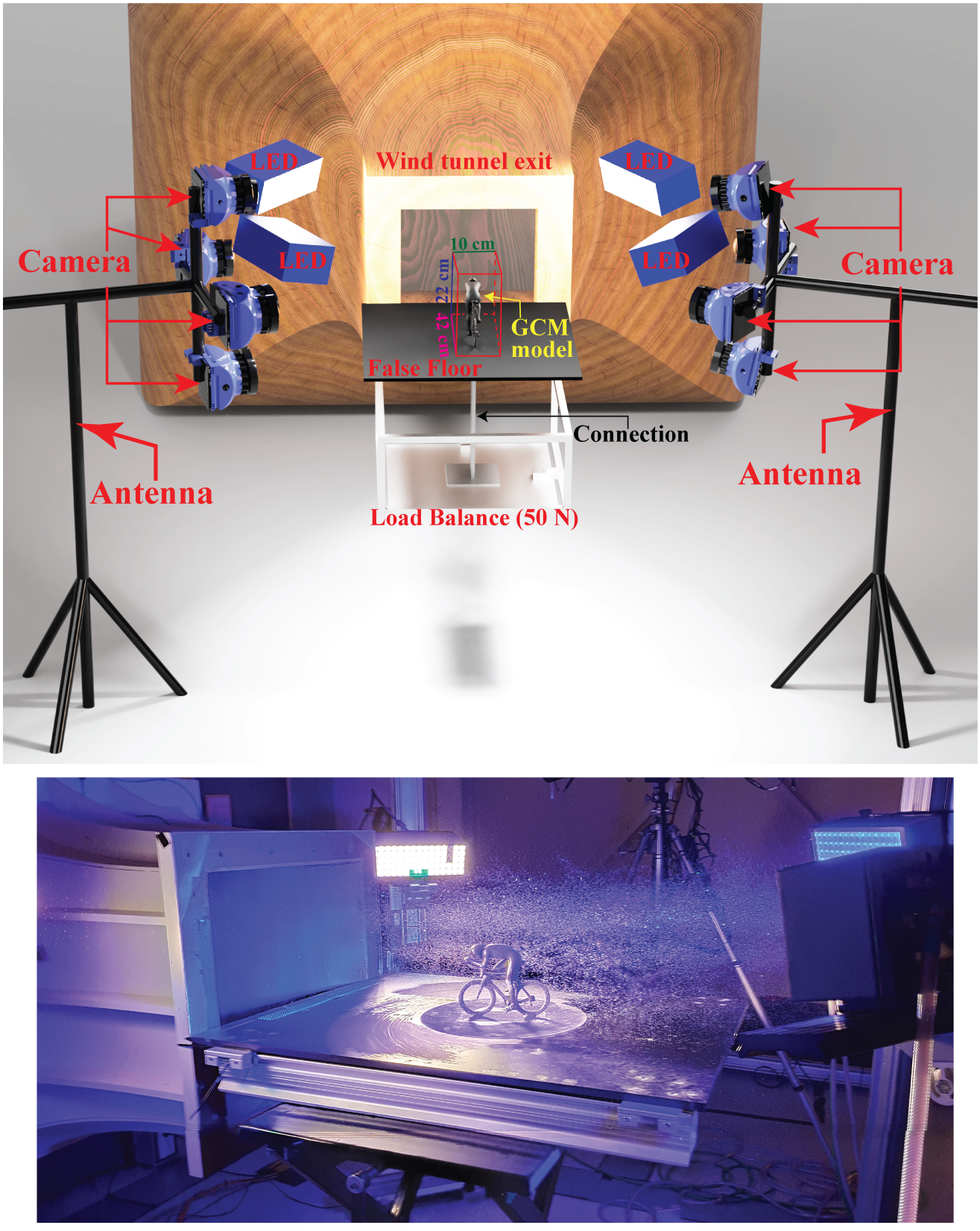


Figure 2. Experimental setup experiment 2: A sketch of the components (Up); a photo illustrating the model and used equipment (Down).

3. Results

3.1. Cylinder flow (2D PIV)

In this section, the flow statistics obtained from Particle Image Velocimetry (PIV) measurements around the cylinder are presented. For 2D PIV, Fig. 3 illustrates the time-averaged lateral and streamwise velocities, the streamwise velocity fluctuations root-mean-square and the time-averaged pressure distributions for the freestream wind speed of 15 m/s and a cylinder with zigzag trip. Fig. 3(A) clearly shows the deceleration of the flow in front of the cylinder which falls to $0.8U_\infty$, the acceleration up to about $1.2V_\infty$ at the upper and lower sides, and the separated wake downstream of the model, with a fluidic reattachment at around $x/D = 2.5$. Beyond this zone, flow velocities in the wake gradually increase recovering towards the freestream velocity. It is worth noting that although the stagnation point exists at the front of the cylinder, it is not visible in the figure. This is attributed to the finite size of the interrogation window, whose linear size is about 14% of the cylinder diameter, thus precluding an accurate evaluation of the velocity at stagnation. In Fig. 3(B), the vertical velocity contours demonstrate a symmetric pattern. Ahead of the cylinder, the flow impinging upon the cylinder divides, directing flow upward toward the upper channel wall and downward toward the lower channel wall. Immediately behind the cylinder, the lower flow ascends while the upper flow descends, driven by the reduced pressure in the wake region. The pressure coefficient distribution around the cylinder, illustrated in Fig. 3(C), is calculated using the formula $C_P = (P - P_\infty)/(0.5\rho U_\infty^2)$, whereby the static pressure P is evaluated via the solution of the Poisson equation for pressure, using Neumann boundary conditions along top, bottom and downstream boundaries, and Dirichlet boundary conditions for the inlet boundary. As expected, the highest pressure occurs at the stagnation point on the cylinder's front face, while the lowest pressure is observed in the immediate wake region, coinciding with the highest reverse-flow velocities. However, due to the limited spatial resolution of the measurement, the maximum C_p attains a value of 0.6 instead of the theoretical value of 1. Further downstream in the wake, pressure recovery occurs, with positive pressures emerging due to flow deceleration caused by the fluidic reattachment at around $x/D = 2.5$ which is in a good agreement with the literature [19]. Lastly, Fig. 3(D) depicts the root mean square (RMS) of the streamwise velocity fluctuations, highlighting maximum RMS values in the cylinder's wake, where the shear layers oscillations induce significant flow fluctuations. As the downstream distance from the cylinder increases, the RMS values diminish due to weakened turbulent activity. It should be noted that two horizontal tripes of relatively high fluctuations ($u_{RMS} \cong 2$ m/s) are present in front of the cylinder, which are attributed to poor illumination due to laser light refraction at the air-cylinder interface. It is remarked that the measured flow fields are in a good agreement with literature [20].

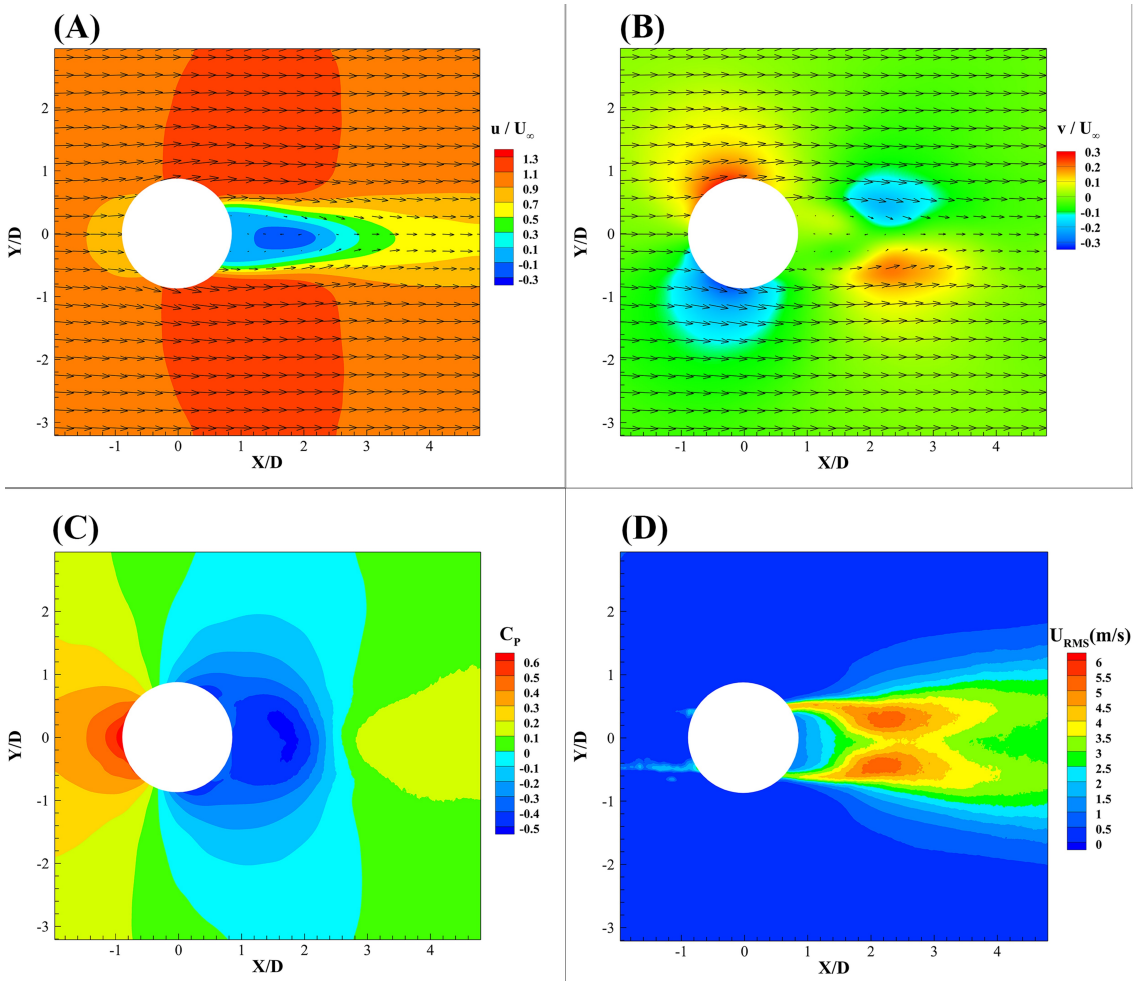


Figure 3. 2D PIV time averaged contours for 15 m/s with zig-zag trip: A) dimensionless u, B) dimensionless v, C) pressure coefficient, and D) root mean square of u.

In Fig. 4(A), the percentage error of the various load-estimation methods relative to the load-balance measurements is presented for the cylinder with zigzag trip and freestream velocity of 15 m/s. For this case, the drag coefficient measured with the load balance was 0.76 which is the value that was used for comparison with PIV data calculations. A blockage correction is omitted, because it affects the measured load through the balance in the same manner as the load estimated using the control volume methods.

For the results presented in Fig. 4, the upstream boundary surface is located $1.84D$ upstream of the cylinder center, while the top and bottom boundary surfaces are positioned $2.6D$ from the center of the cylinder. The downstream surface is not fixed; instead, it moves, as indicated along the horizontal axis. The origin of the coordinate system is defined at the center of the cylinder. As shown in the results, the control-volume (CV) method exhibits an error of approximately 10% at $X/D = 1$, which decreases monotonically with downstream distance and falls below 1% for $X/D > 4.5$. In contrast, the wake-rake method starts with an error of about 5% at $X/D = 1.5$, initially increases

to approximately 6% around $X/D = 1.7$, and then decreases continuously, eventually becoming negative and reaching an error of about -8% at the downstream end of the measurement domain. The CPT method follows a similar downstream trend to the wake-rake approach but with a systematic offset. Moreover, this method provides real number estimates only once the pressure has recovered to the freestream value, in accordance with its underlying assumption. Owing to its positive offset relative to the wake-rake method, the CPT error is reduced to approximately -4% at the end of the domain. Another source of error for the wake-rake method, compared with the CV method, is its reliance on the assumption that the contributions of the upper and lower control surfaces are negligible or, in other terms, that the velocity and pressure have reached the freestream values at the top and bottom of the wake rake. The wake-rake method matches the CV result only if the contributions of upper and lower control surfaces are effectively zero. However, Fig. 4(B) demonstrates that, although the influence of the upper and lower surfaces is substantially smaller than that of the downstream surface, it is not negligible (this figure is plotted by dividing the surfaces momentum to the left surface's and due to the fact that the flow is not completely 2D the sum of the contributions in total cannot get 100%). In particular, the bottom surface contributes a few percentages to the total integrated drag; its contribution is higher than that of the top surface primarily due to lack of perfect flow symmetry between the upper and lower wind-tunnel walls. Consequently, even with a control-volume width approximately five times the cylinder diameter, the upper and lower surface contributions do not vanish. Also it can be seen that the up and down surface added together can have around 7% contribution which was close to the final error of the wake rake method.

The CPT method does not yield valid results within the first three diameters downstream of the cylinder because, its formulation contains a square-root term that becomes undefined when the argument is negative. This occurs because the assumption that the static pressure in the wake has recovered to the freestream value is violated. Once valid values appear, the CPT method shows the similar trend as the wake-rake method, although with smaller errors. However, the fact that the error of the CPT method is smaller than that of the wake rake method is purely ascribed to the fact that, in this region of the wake ($x/D > 3/5$), the static pressure is positive: by assuming that the static pressure is equal to the freestream value, the CPT method is effectively biasing the drag results to higher values than the wake rake approach. Similar to the wake-rake approach, the accuracy of the CPT method is strongly influenced by the prescribed freestream conditions; for consistency, identical upstream PIV-derived freestream values were used for both methods.

The errors associated with both the wake-rake and CPT methods are highly sensitive to the prescribed freestream pressure and velocity. Even a 1% variation in the freestream velocity can lead to a substantial change in the computed error, as shown in Fig. 5. Both methods exhibit very similar sensitivity to U_∞, and both are considerably more sensitive to U_∞ than to P_∞. Moreover, the sensitivity to U_∞ varies with the magnitude of the imposed velocity bias, whereas the sensitivity to P_∞ remains approximately constant. This behavior is mainly due to the different roles of U_∞ and P_∞

in the expression for C_D. The freestream velocity appears squared in the denominator of C_D, while it also appears linearly in the numerator. In contrast, P_∞ appears only linearly in the numerator; therefore, the sensitivity to errors in P_∞ is approximately linear, as observed in Fig. 5(B). Another important observation is that the sensitivity is higher for negative errors in U_∞ than for positive errors. This asymmetry occurs because, in the numerator of the C_D expression, U_∞ is subtracted from the local flow velocity. Therefore, when the imposed error in U_∞ is negative, the contribution of the velocity-related term to C_D increases, resulting in a larger error in the computed drag coefficient.

Overall, these results indicate that the wake-rake and CPT methods will always underestimate the aerodynamic drag of a bluff body in close proximity to the body, and achieving an accuracy comparable to the CV method requires a substantially larger measurement domain, which is often not feasible in PIV setups. Using smaller domains, these methods might still be valuable to use to obtain relative drag differences between objects of different shape or surface roughness, in cases where the absolute aerodynamic drag is of less importance.

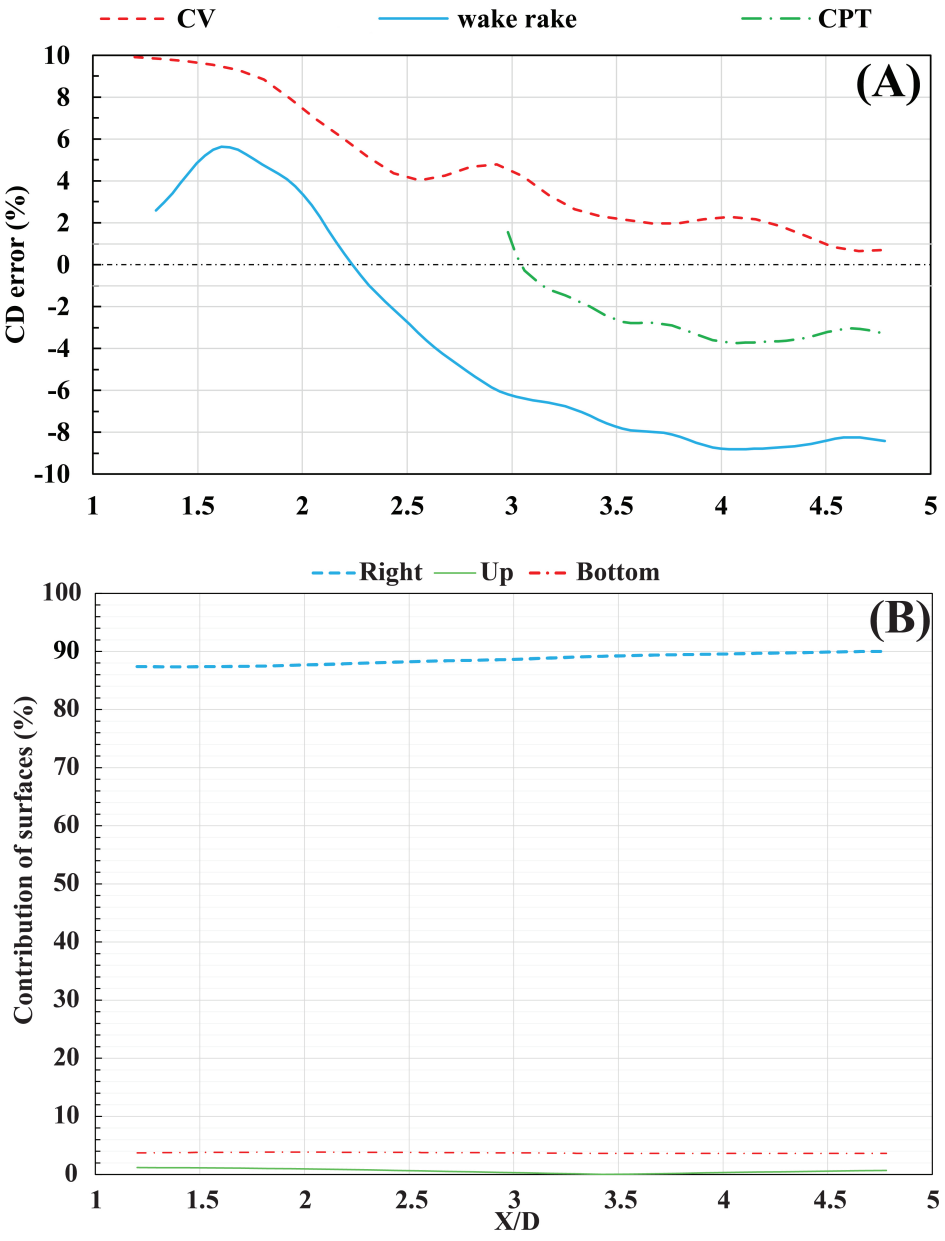


Figure 4. A) Error of different methods of drag coefficient calculation for 15 m/s with zig-zag trip and B) contribution of the different surfaces of the CV method to the overall drag.

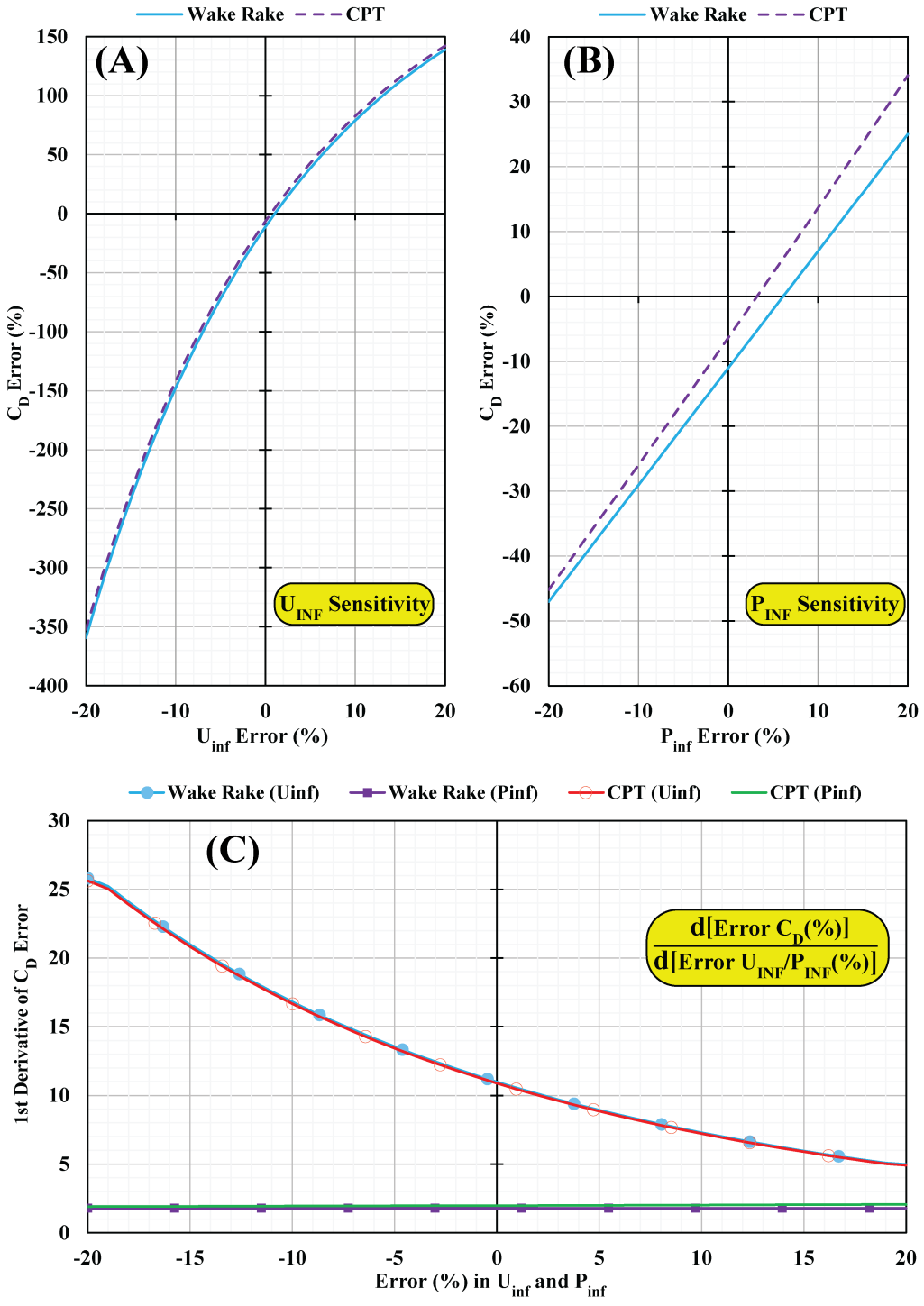


Figure 5. Sensitivity of the wake-rake and CPT methods to bias errors in P_∞ and U_∞ and the dependence of this sensitivity on the magnitude of the imposed bias error.

3.2. Flow around the cyclist (3D LPT)

In this section, the results based on the 3D LPT measurements around the scaled cyclist model are presented. Fig. 6 illustrates the velocities in different planes as well as some streamlines around the cyclist. In right side of the figure, control volume boundaries are brought. The planes' distance from the front end of the bike are normalized regarding bike length and brought above each figure. The presented results are in a good agreement with the same contours in the literature [21]. In this figure low velocity region around the cyclist body can be seen and also the wake of the cyclist can be seen in the end plane ($X/L = 1.25$). Also, it can be found that the velocities recover to the freestream velocity in a small distance from the cyclist body. It can be seen that streamlines closer to the cyclist are more affected and they are not as straight as others which are far from the body. Overall, the extracted results show very good agreement with previously reported flow features around cyclists, confirming the reliability of the present PIV dataset [21].

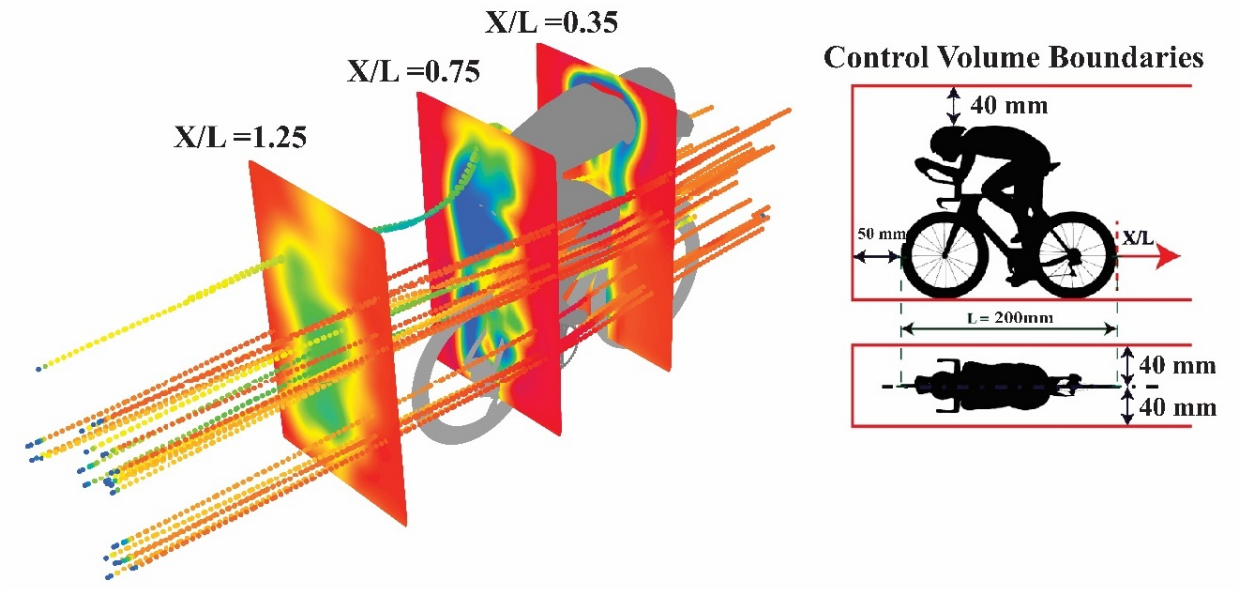


Figure 6. Iso-surfaces of the time-averaged streamwise vorticity component around the scaled cyclist model.

Using the 3D LPT data and the previously introduced methods, the drag coefficient of the scaled cyclist model was calculated, and the error of the results compared to the load balance are presented in Fig. 7. The dimensions of the control volume are depicted in Fig. 6. The horizontal axis in this figure represents the distance downstream of the rear wheel, normalized by the total bicycle length ($L = 0.2$ m).

As shown in Fig. 7, similar to the 3D results, the CV method again provides the best performance in terms of accuracy. Close to the object, it starts with a small negative error of approximately 1%. The error then initially increases, before decreasing to below 1%, where it remains until the end of the x-axis, corresponding to locations further downstream of the object.

The wake-rake and CPT methods show similar trends, with the wake-rake method producing slightly smaller errors. Both methods underestimate the drag coefficient, as also observed for the 2D PIV case. Their errors are approximately 5%, and although their fluctuations' range are close to those of the CV method, they exhibit a more robust trend.

It should be noted that the sensitivity of these methods to the freestream pressure and velocity, P_∞ and U_∞, again plays an important role, similar to the 2D case. Although the drag coefficients obtained using the CV method fluctuate around 0% error toward the end of the measurement domain, the wake-rake and CPT methods exhibit continuously decreasing trends. These trends are almost identical, with only a small gap between their values, indicating that these methods have not yet converged within the available measurement domain and would require measurement planes located further downstream. This again highlights the advantage of the CV method, which requires a much smaller measurement domain for load estimation.

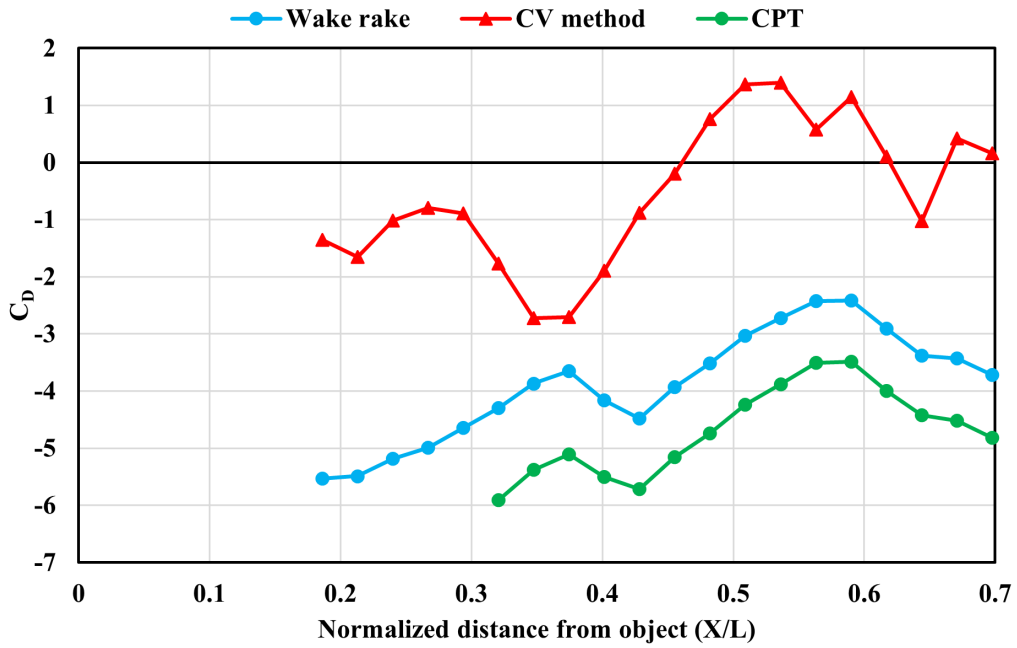


Figure 7. C_D error computed from 3D LPT data compared to the load balance results around the scaled cyclist model, as a function of the location of the downstream boundary of the control volume.

4. Conclusion

In this study, two and three dimensional PIV and LPT measurements were performed around a transparent cylinder and a scaled cyclist model, respectively. The measured velocity fields were subsequently used to compute the aerodynamic drag values using three load estimation methods, namely the control volume approach, the wake rake approach and the total pressure coefficient method. The drag results will then be compared with the measurements from load balances

connected to the wind tunnel models. This allows the accuracy of the different drag-estimation methods for a bluff body to be evaluated for various sizes of the measurement domain. The main conclusions derived from the results are summarized below:

- All force-estimation methods considered in this study require pressure information, which cannot be obtained directly from PIV and LPT measurements. The pressure reconstruction step introduces additional uncertainty, particularly in regions where velocity gradients and fluctuations are small.
- The results from planar PIV are affected by the three-dimensionality of the flow. For the cylinder flow experiment, the errors of the estimated drag coefficient are the largest when the downstream plane is located within a distance of two diameters from the cylinder center. After that distance, the flow becomes essentially two-dimensional and the errors of the drag coefficient reduce.
- The results indicate that the wake-rake and CPT methods are not suitable for large-scale objects, as they require flow-field data over regions considerably larger than the characteristic dimensions of the object. For large bodies, acquiring such extensive PIV measurements either in a large plane or volume may not be practically feasible.
- Overall, obtaining accurate force estimates from PIV data involves a trade-off between measuring a very large region only downstream of the object or a smaller region that fully encloses the body. When a small downstream region is measured, the error in force estimation from 2D PIV can easily exceed 10%, even for a simple bluff body such as a cylinder.
- One of the advantages of the CPT and wake-rake methods reported in the literature is that they require fewer measurement surfaces. However, these methods rely on the freestream pressure and velocity, P_∞ and U_∞, and are highly sensitive to these quantities, particularly U_∞. Therefore, accurate measurement of the freestream pressure and velocity is essential to obtain reliable results. If these values are only roughly estimated or assumed, the final accuracy can be significantly affected, making the results less reliable.
- For the 3D LPT results, although all methods yield nearly identical errors, the CV method stabilizes faster than the wake-rake method and fluctuates around 0% error. In contrast, the CPT and wake-rake methods do not reach a constant value within the measurement domain; instead, their errors continue to decrease toward zero until the end of the domain. This indicates that these methods require measurement planes located further downstream of the object to stabilize. Therefore, they require not only a larger measurement surface but also a measurement domain extending farther downstream compared with the CV method.

References

[1] J. Perez-Ramirez and E. V. Kondratenko, "Evolution, achievements, and perspectives of the TAP technique," *Catalysis Today*, vol. 121, no. 3–4, pp. 160–169, Mar. 2007, doi:10.1016/J.CATTOD.2007.01.001.

[2] E. A. Pifer and G. Bramesfeld, "Measuring Wing Profile Drag using an Integrating Wake Rake," *Technical Soaring*, vol. 36, no. 3, pp. 74–82, 2012, Accessed: Nov. 01, 2024. [Online]. Available: `https://journals.sfu.ca/ts/index.php/ts/article/view/289`

[3] B. W. Van Oudheusden, F. Scarano, and E. W. F. Casimiri, "Non-intrusive load characterization of an airfoil using PIV," *Experiments in Fluids*, vol. 40, no. 6, pp. 988–992, Jun. 2006, doi: 10.1007/s00348-006-0149-2.

[4] B. W. Van Oudheusden, F. Scarano, E. W. M. Roosenboom, E. W. F. Casimiri, and L. J. Souverein, "Evaluation of integral forces and pressure fields from planar velocimetry data for incompressible and compressible flows," *Experiments in Fluids*, vol. 43, no. 2–3, pp. 153–162, Aug. 2007, doi: 10.1007/s00348-007-0261-y.

[5] E. Limacher, C. Morton, and D. Wood, "On the calculation of force from PIV data using the generalized added-mass and circulatory force decomposition," *Experiments in Fluids*, vol. 60, no. 1, Jan. 2019, doi: 10.1007/s00348-018-2648-3.

[6] K. Gharali and D. A. Johnson, "PIV-based load investigation in dynamic stall for different reduced frequencies," *Experiments in Fluids*, vol. 55, no. 8, 2014, doi: 10.1007/s00348-014-1803-8.

[7] A. Villegas and F. J. Diez, "On the quasi-instantaneous aerodynamic load and pressure field measurements on turbines by non-intrusive PIV," *Renewable Energy*, vol. 63, pp. 181–193, Mar. 2014, doi: 10.1016/j.renene.2013.09.015.

[8] N. Fujisawa, S. Tanahashi, and K. Srinivas, "Evaluation of pressure field and fluid forces on a circular cylinder with and without rotational oscillation using velocity data from PIV measurement," *Measurement Science and Technology*, vol. 16, no. 4, pp. 989–996, 2005, doi: 10.1088/0957-0233/16/4/011.

[9] W. Terra, A. Sciacchitano, and Y. H. Shah, "Aerodynamic drag determination of a full-scale cyclist mannequin from large-scale PTV measurements," *Experiments in Fluids*, vol. 60, no. 2, pp. 29-, Jan. 2019, doi: 10.1007/S00348-019-2677-6.

[10] B. W. Van Oudheusden, E. W. F. Casimiri, and F. Scarano, "Aerodynamic load measurement of a low speed airfoil using particle image velocimetry," *45th AIAA Aerospace Sciences Meeting and Exhibit*, vol. 1, pp. 444–451, 2007, doi: 10.2514/6.2007-49.

[11] B. W. Van Oudheusden, "PIV-based pressure measurement," *Measurement Science and Technology*, vol. 24, no. 3, p. 032001, Jan. 2013, doi: 10.1088/0957-0233/24/3/032001.

[12] W. Terra, A. Sciacchitano, F. Scarano, and B. W. van Oudheusden, "Drag resolution of a PIV wake rake for transiting models," *Experiments in Fluids*, vol. 59, no. 7, pp. 1–6, Jul. 2018, doi: 10.1007/S00348-018-2570-8/TABLES/1.

[13] "Measurement of profile drag by the Pitot-Traverse method - Google Scholar." Accessed: Oct. 15, 2024. [Online]. Available: `https://scholar.google.com/scholar?hl=en&as_sdt=0%2C5&q=Measurement+of+profile+drag+by+the+Pitot-Traverse+method&btnG=`

[14] N. Timmer and L. Veldhuis, "The Impact of Skinsuit Zigzag Tape Turbulators on Speed Skating Performance," *Applied Sciences*, vol. 11, no. 3, pp. 1–18, Jan. 2021, doi: 10.3390/APP11030988.

[15] S. Abdallah, "Numerical solutions for the pressure Poisson equation with Neumann boundary conditions using a non-staggered grid, I," *Journal of Computational Physics*, vol. 70, no. 1, pp. 182–192, May 1987, doi: 10.1016/0021-9991(87)90008-8.

[16] M. Huang, A. Sciacchitano, and C. Ferreira, "On the wake deflection of vertical axis wind turbines by pitched blades," *Wind Energy*, vol. 26, no. 4, pp. 365–387, Apr. 2023, doi: 10.1002/we.2803.

[17] L. A. Hendriksen, A. G. Guerra, A. Sciacchitano, and F. Scarano, "Omnidirectional Particle Image Velocimetry," 2025.

[18] M. Novara, D. Schanz, and A. Schroder, "Two-Pulse 3D particle tracking with Shake-The-Box," *Experiments in Fluids*, vol. 64, no. 5, pp. 93-, Apr. 2023, doi: 10.1007/S00348-023-03634-7.

[19] S.-J. Lee, "Numerical Simulation of Vortex-Dominated Flows Using the Penalized VIC Method," *Vortex Dynamics and Optical Vortices*, Mar. 2017, doi: 10.5772/65371.

[20] P. Catalano, M. Wang, G. Iaccarino, and P. Moin, "Numerical simulation of the flow around a circular cylinder at high Reynolds numbers," *International Journal of Heat and Fluid Flow*, vol. 24, no. 4, pp. 463–469, Aug. 2003, doi: 10.1016/S0142-727X(03)00061-4.

[21] W. Terra et al., "A Generic Cyclist Model for aerodynamic investigation: Design, geometry & first aerodynamic analysis of a male time-trial and sprint model," *Journal of Wind Engineering and Industrial Aerodynamics*, vol. 252, p. 105829, Sep. 2024, doi: 10.1016/J.JWEIA.2024.105829.